Electric Power Components and Systems

ISSN: (Print) (Online) Journal homepage: https://www.tandfonline.com/loi/uemp20

Analytical Performance Estimation of a Fall-Back Inner-Rotor Transverse-Flux Permanent Magnet Generator using Magnetic Equivalent Reluctance Circuit

Mahesh A. Patel & Santosh C. Vora

Electric Power Components and Systems, 0(0): 1–13, 2023

ISSN: 1532-5008 print / 1532-5016 online
DOI: 10.1080/15325008.2023.2180694

Analytical Performance Estimation of a Fall-Back Inner-Rotor Transverse-Flux Permanent Magnet Generator using Magnetic Equivalent Reluctance Circuit

Mahesh A. Patel and Santosh C. Vora
Department of Electrical Engineering, Institute of Technology, Nirma University, Ahmedabad, Gujarat, India

CONTENTS

1. Introduction
2. A Novel FB-TFPMG
3. MERC of FB-TFPMG
4. Result and Discussion
5. Conclusion
References

Abstract—The potential of wind energy resources is propelled fast and power extraction is increasing considerably due to the development of reliable and cost-effective wind turbine generators. Various permanent magnet (PM) wind generators have been implemented for wind power generation, among which, the conventional transverse-flux permanent magnet generator (TFPMG) is popular due to their higher torque density and simple coil design, but it has some disadvantages in comparison with radial flux PM generator, i.e., higher flux leakages and complex 3D flux pattern. In this article, a fall-back inner rotor transverse-flux PM wind generator FB-TFPMG has been investigated to override the disadvantages of conventional TFPMG. It employs half of the total PMs on the rotor and U-shaped stator cores. An analytical model of the proposed FB-TFPMG has derived using magnetic equivalent reluctance circuit (MERC) to predict the performance of the generator, i.e., flux densities in the air-gap, under aligned and unaligned conditions of rotor PMs with U-shaped stator cores. The results of the MERC model is verified with the results obtained through 3D finite element analysis.

1. INTRODUCTION

The priority for generating power has shifted to a great extent to renewable energy sources such as solar and wind energy. Among renewable energy sources, wind energy has attracted a lot of attention due to advancements in wind generator technologies [1, 2]. The key objective of the developments is to explore the relevant generator system for overall performance improvement. For a decade, various wind generation concepts with different PM generator designs [3–5] have been developed and proposed to improve efficiency, reduce size of the system, costs, and better power quality. Direct-drive permanent magnet (PM) generators are suitable for large-capacity of wind power plants; are reliable, have longer life, improved performance with lower maintenance, lower

Keywords: fall-back rotor, magnetic equivalent reluctance circuit, permanent magnet machines, renewable energy sources, transverse-flux, wind energy, wind generator
Received 15 February 2022; accepted 4 February 2023

Address correspondence to Santosh C. Vora, Department of Electrical Engineering, Institute of Technology, Nirma University, Ahmedabad, Gujarat 382481, India. E-mail: santoshvora@yahoo.com

capital cost, and less weight [6–9]. A comparison of different generator topologies [10–13] has been carried out and among all, the conventional transverse-flux PM generator (TFPMG) is emerging as a suitable direct-drive wind generator due to its high torque density [14–16] and simple coil structure. Various topologies of TFPM generator have been reviewed, viz., single-sided and double-sided TFPMG [17], with surface-mounted and inset-mounted PM [18], the inner-rotor and outer-rotor [19] TFPMG, flux-concentrating TFPMG [20], claw-pole TFPMG [21], C-core, U-core [22], and E-core TFPMG [23]. The modeling methods, i.e., magnetic equivalent circuit [24], finite-element analysis models [25], harmonic method and magnetic charge method [26] have been discussed in the literature to model the TFPM generators. The major limitations of conventional TFPMG are complex design, uneven magnetic flux distribution, and high leakage flux due to multi-dimensional magnetic flux pattern. Due to the larger size and mass of the TFPM generators, the total cost and the operational issues are two primary factors to be resolved by inventing new topologies. In conventional TFPMG, only half of the employed PMs are effectively participating in the energy conversion process [27]. The iron bridges are the alternatives inserted between nearby stator cores, to restrict the excessive large leakage flux. This flux leakage initiates the additional current in the iron bridge, which reduces the effective flux linkage, contributes to increased power loss and lowering the efficiency of the machine slightly. Various magnetic equivalent circuits [24, 28–31] have been studied for various topologies of TFPMGs to predict the performance of the generator.

A fall-back transverse-flux permanent-magnet generator (FB-TFPMG) with an inner rotor design has been compared with conventional TFPMG in Refs. [25, 32], which employs half the number of PMs (as against conventional TFPMG), elliptical shaped stator core and toroidal-shaped coil. Fall-back path of the rotor offers certain advantages i.e., it reduces the losses due to the elimination of inactive magnets and therefore overall performance of the generator is improved. In this article, an analytical design using a magnetic equivalent reluctance circuit (MERC) of TFPMG with a concept of a fall-back rotor is derived to predict the flux densities in the air-gap and other parts of the generator. A formulation for sizing equation and initial design parameters of the FB-TFPMG have been discussed. MERC model takes less time in comparison with finite element analysis. Reluctances and hence the fluxes of various parts of the generator are computed using PM's equivalent mmfs and compared with the results obtained from the 3D FE analysis.

In this article, a basic structure of the inner rotor FB-TFPMG is briefly recalled in Section 2 and preliminary equations of main dimensions are derived. A MERC of FB-TFPMG is derived in the Section 3 under different rotor positions. The induced emf and flux density plots obtained through the finite element analysis tool of the inner rotor FB-TFPMG, are presented in Section 4. The air-gap flux density of the inner rotor FB-TFPMG under different rotor positions is compared with the flux density calculated by analytical means, i.e., MERC. The conclusion is presented in Section 5.

2. A NOVEL FB-TFPMG

2.1. Structure of the FB-TFPMG

The single-phase structure of a FB-TFPMG is shown in Figure 1. The difference between the conventional TFPMG and the FB-TFPMG, is that the active magnets are only employed in the FB-TFPMG and inactive magnets are replaced by the concept of a fall-back rotor. A stator core is made of iron with an even number of elliptical U-shaped stator poles placed circumferentially around the rotor assembly. Due to the elliptical shape of stator cores and the toroidal shape of the coil, the active mass of the material is reduced. A rotor contains a number of PM pole pairs equal to the number of stator cores. The flux diverted through the fall-back path of the rotor serves the purpose of inactive magnets. N_dF_eB magnets are used for the rotor poles.

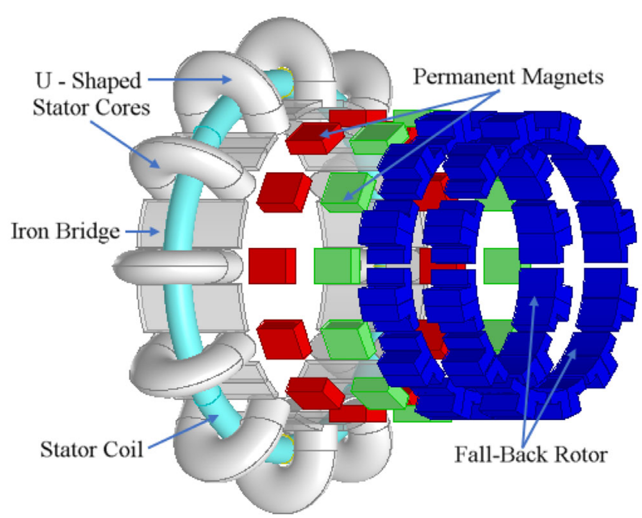

FIGURE 1. A construction of fall-back transverse-flux PM generator (FB-TFPMG).

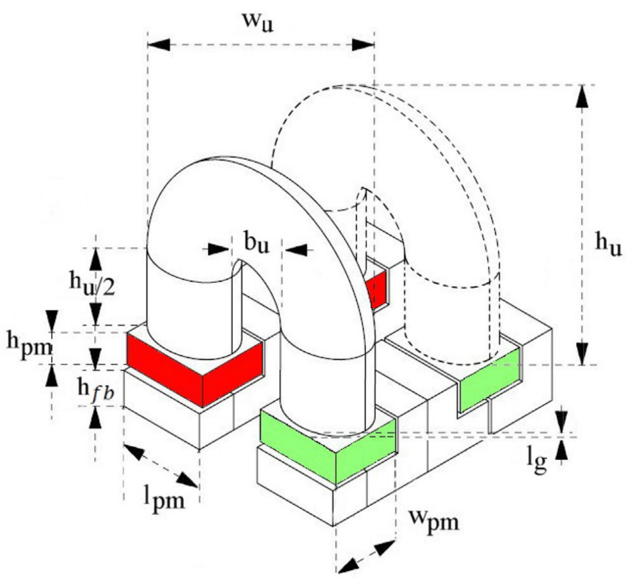

FIGURE 2. A cut section of inner rotor FB-TFPMG (Single phase representation).

A detailed cut-section of single phase inner rotor FB-TFPMG is represented with their dimensional notations in Figure 2, where l_{pm} is the axial length of the PM, w_{pm} is the width of the PM, h_{pm} is the height of the PM, w_u is the axial width of the stator core per phase, h_u is the height of the stator core, h_{fb} is the height of the rotor yoke, and l_g is the air-gap length.

2.2. Determination of Design Dimensions of FB-TFPMG

The PM dimensions are calculated for the determination of overall performance of the generator. This section determines the main dimensions of the proposed inner-rotor FB-TFPMG. Various dimensions, i.e., magnet dimensions, rotor pole pitch, rotor and stator diameters, and length of generator are required for analytical calculations. The height of the magnet relies on the properties of the magnetic material and flux density in the air-gap. In a magnetic circuit, a stator core and two PMs are used for one pole pair. The flux density over the inactive fall-back rotor is half of the flux density under the stator core area due to the flux that pass through each stator U-core is divided between two adjacent area over the fall-back rotor for the completion of the magnetic flux path. All the calculations are done for a 1 kW, 300 rpm FB-TFPMG with 12 stator cores. N40 N_dF_eB PMs are employed with a remanent flux density is 1.25 T. For the calculation of magnet height, a half section of stator pole and a PM is considered. According to Ref. [18], the Ampere's Law equation becomes,

$$H_m.h_{pm} + H_g.l_g = 0 \tag{1}$$

where H_m is field intensity inside the PM and h_{pm} is height of the magnet, H_g is the air-gap field intensity, and l_g is the air-gap length. The h_{pm} can be obtained by,

$$h_{pm} = \frac{B_r.B_g.l_g}{\mu_0|H_c|(B_{r(pm)} - B_g)} \tag{2}$$

where $B_{r(pm)}$ is the remanent flux density of PMs, H_c is the coercive force, and B_g is the air-gap flux density.

As the PM pole pitch decreases with a large number of poles, the PM fringing flux increases. The PM pole pitch τ_{pm} should be higher than total of PM height plus actual air-gap to minimize the fringing flux [33]. The rotor PM pole pitch τ_{pm} can be calculated by,

$$\tau_{pm} = \frac{\pi.D_{rt,o}}{p} \tag{3}$$

where $D_{rt,o}$ is the outer diameter of the rotor and p is the total number of poles.

Stack length of the machine is determined by assuming a suitable ratio (k) of stack length to diameter (0.2–0.4). The assumption is based on designer's choice, which can determine the proportion of the generator dimensions.

$$L_{st} = k.D_{st,i} \tag{4}$$

where L_{st} is the stack length of the rotor, and $D_{st,i}$ is stator inner diameter of the machine. The stator outer diameter $D_{(st,o)}$ is computed by adding the height of the elliptical shaped stator core h_u and h_{sy},

$$D_{st,o} = D_{st,i} + h_u + h_{sy} \tag{5}$$

where $D_{(st,o)}$ is the stator outer diameter, h_u is the height of U-stator core, and h_{sy} is stator yoke height. Initial design parameters are tabulated in Table 1.

3. MERC OF FB-TFPMG

In this section, an analytical modeling using MERC is discussed to design inner rotor FB-TFPMG. The individual reluctance of the air-gap, elliptical shaped U-stator core, fall-back rotor and rotor PM poles is required for the development of the MERC. The magnetic flux direction in fall-back rotor pole and the PM is in the opposite direction. The fluxes due to PMs, pass through the stator core in one direction and after rotation of a pole pitch, the flux passes through the stator core in the reverse direction from the fall-back rotor part. Therefore, the calculation of the flux

Parameters	Values (mm)
Height of PM (h_{pm})	6.23
Width of PM (w_{pm})	13
Length of PM (l_{pm})	18
Average diameter of the air-gap (D_g)	120
Rotor outer diameter (D_{rout})	119
Stator inner diameter (D_{sin})	121
Distance between stator poles (b_u)	12
Axial stack length of the FB-TFPMG (w_u)	48
Height of the stator core (h_u)	33
Height of the fall-back rotor (h_{fb})	6.5
Rotor PM pole pitch (τ_{pm})	15.5
Air-gap	1
No. of rotor poles (active and fall-back)	12 + 12
No. of stator cores	12
Magnetic flux density in air-gap	0.9 T
Number of turns per coil per phase	24

TABLE 1. Design parameters of inner rotor FB-TFPMG.

and flux density is essential in the air-gap for various rotor positions. In the proposed MERC, reluctances of different parts of the FB-TFPMG, corresponding to the flux path have been calculated and the reluctance matrix is developed according to Ref. [34]. Magnetic fluxes are determined with the help of mmf sources. The flux densities in all the parts of FB-TFPMG have been enumerated according to Ref. [35]. The electromagnetic characteristics of each rotor pole pair is the same and repetitive for all other pairs of FB-TFPMG. Therefore, a 3D model of one pole pair is derived for MERC based analytical model of the proposed FB-TFPMG as depicted in Figure 3. The sources of the magnetic flux are distributed through air-gap and these fluxes are linked with the stator core, which are also diverted through the fall-back rotor path and iron bridges. The MERC is derived for two different rotor positions, i.e., aligned condition and unaligned conditions as described below.

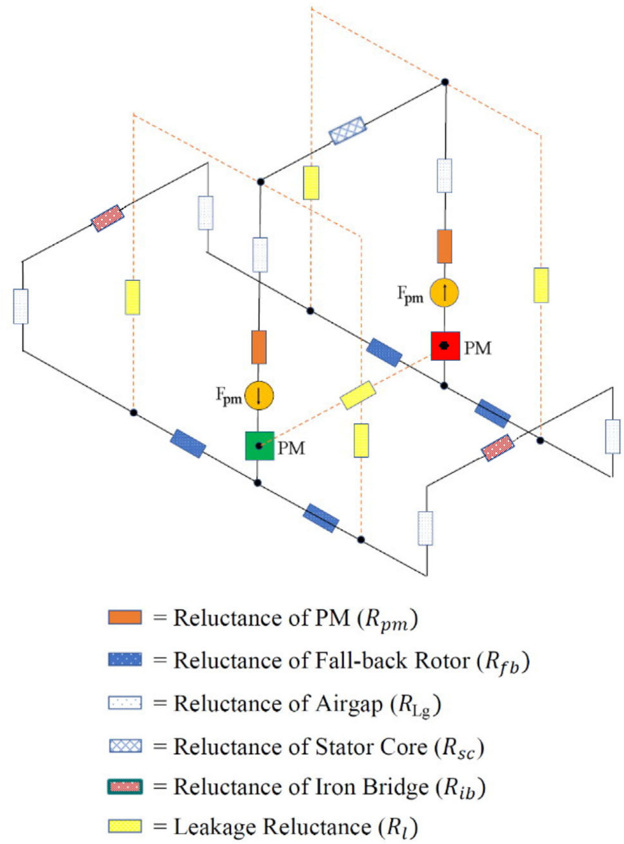

FIGURE 3. Magnetic equivalent reluctance circuit (MERC) of FB-TFPMG.

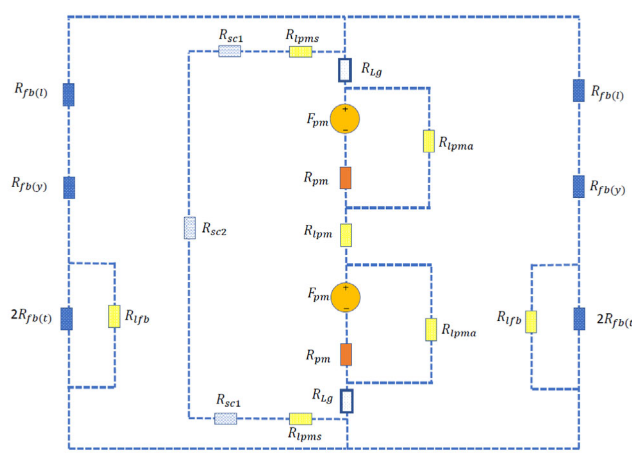

FIGURE 4. MERC of FB-TFPMG under aligned condition.

3.1. MERC under Aligned Condition

In aligned condition, the elliptical shaped stator core is considered exactly under the rotor active PMs pole, and half of the fall-back rotor parts from both the side are considered for the development of the magnetic circuit of one pole pair. A magnetic equivalent circuit of FB-TFPMG under aligned condition of rotor PM poles with elliptical U-shaped stator core is shown in Figure 4 and the simplified MERC is depicted in Figure 5. Various leakage reluctances, i.e., R_{lpm} (reluctance offered to flux between two active PMs), R_{lpma} (self reluctance of a PM), R_{lpms} (lateral leakage fluxes between fall-back rotor part and elliptical U-shaped stator core), and R_{lfb} (leakage fluxes due to fall-back rotor) are represented in the circuit. The PM's mmf sources are also modeled with their own reluctance. Using the simplified magnetic circuit, and Kirchhoff's law all fluxes and flux densities are derived for various parts of

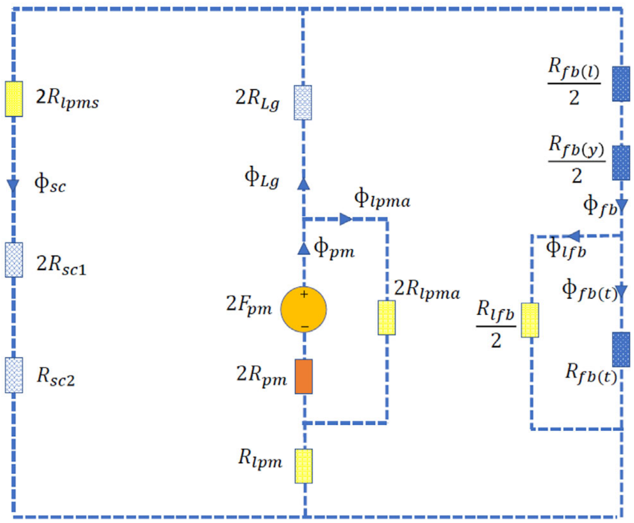

FIGURE 5. Simplified MERC of FB-TFPMG.

FB-TFPMG, i.e., the different parts of fall-back rotor, the stator core length, air-gap, and leakage fluxes in aligned condition. Based on the circuit shown in Figure 5, the following equations have been derived.

$$\left.\begin{aligned}
R_{pm}\phi_{pm} + R_{lpma}\phi_{lpma} = F_{pm}\\
2R_{pm}\phi_{pm} + (2R_{lg} + R_{lpm})\phi_{lg} + (2R_{sc1}+\\
R_{sc2} + R_{lpms})\phi_{sc} = 2F_{pm}\\
\phi_{pm} - \phi_{lg} - \phi_{lpma} = 0\\
\phi_{lg} - \phi_{sc} - \phi_{fb} = 0\\
2R_{pm}\phi_{pm} + (2R_{lg} + R_{lpm})\phi_{lg} - (R_{fb(l)}/2+\\
R_{fb(y)}/2 + R_{fb(t)})\phi_{fb} = 2F_{pm}\\
\phi_{fb} - \phi_{lfb} - \phi_{fb(t)} = 0\\
R_{fb(t)}\phi_{fb(t)} - (R_{lfb}/2).\phi_{lfb} = 0
\end{aligned}\right\} \tag{6}$$

These equations can be written in the matrix form under aligned condition,

$$\begin{bmatrix} R_{11} & 0 & 0 & 0 & R_{15} & 0 & 0\\ R_{21} & R_{22} & R_{23} & 0 & 0 & 0 & 0\\ 1 & -1 & 0 & 0 & -1 & 0 & 0\\ 0 & 1 & -1 & -1 & 0 & 0 & 0\\ R_{51} & R_{52} & 0 & R_{54} & 0 & 0 & 0\\ 0 & 0 & 0 & 1 & 0 & -1 & -1\\ 0 & 0 & 0 & 0 & 0 & R_{76} & R_{77} \end{bmatrix} \begin{bmatrix} \Phi_{pm}\\ \phi_{lg}\\ \phi_{sc}\\ \phi_{fb}\\ \phi_{lpma}\\ \phi_{lfb}\\ \phi_{fb(t)} \end{bmatrix} = \begin{bmatrix} F_{pm}\\ 2F_{pm}\\ 0\\ 0\\ 2F_{pm}\\ 0\\ 0 \end{bmatrix} \tag{7}$$

where $R_{11} = R_{pm}$, $R_{15} = R_{lpma}$, $R_{21} = R_{51} = 2R_{pm}$, $R_{22} = R_{52} = 2R_{lg} + R_{lpm}$, $R_{23} = 2R_{sc1} + R_{sc2}$ $R_{54} = (R_{fb(l)}/2 + R_{fb(y)}/2 + +R_{fb(t)})$, $R_{76} = -R_{lfb}/2$, and $R_{77} = R_{fb(t)}$

3.2. MERC under Unaligned Condition

In unaligned condition, the elliptical shaped stator core is considered exactly under fall-back rotor pole, and at the same time half of the rotor PMs from both the sides are considered for the development of magnetic circuit of a pole pair. A magnetic equivalent circuit of FB-TFPMG under unaligned condition of fall-back rotor poles with elliptical U-shaped stator core is shown in Figure 6 and a simplified MERC is depicted in Figure 7.

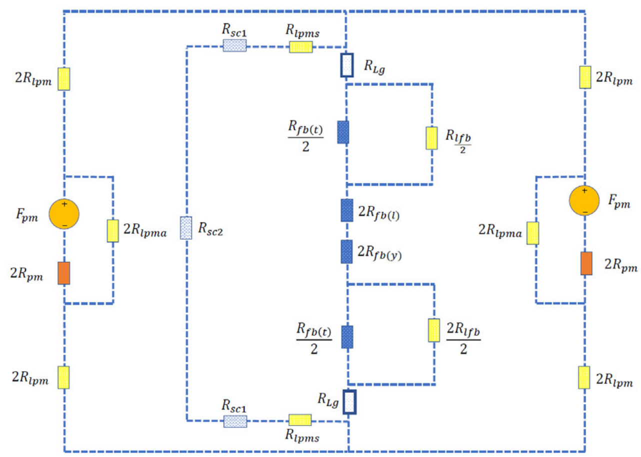

FIGURE 6. MERC of FB-TFPMG under unaligned condition.

Similarly, using simplified magnetic circuit, it is necessary to write a set of equations to find all fluxes and flux densities in different parts of FB-TFPMG, i.e., different parts of fall-back rotor, the stator core length, air-gap, and leakage fluxes in unaligned condition. Following equations are derived based on the circuit shown in Figure 7.

$$\left.\begin{aligned}
R_{pm}\phi_{pm} + R_{lpma}\phi_{lpma} = F_{pm}\\
R_{pm}\phi_{pm} + R_{lg}\phi_{lg}\\
+(2R_{sc1} + R_{sc2} + R_{lpms})\phi_{sc} = F_{pm}\\
\phi_{pm} - \phi_{lg} - \phi_{lpma} = 0\\
\phi_{lg} - \phi_{sc} - \phi_{fb} = 0\\
R_{pm}\phi_{pm} + R_{lg}\phi_{lg} - (2R_{lpm} + R_{fb(l)}\\
+R_{fb(y)} + R_{fb(t)})\phi_{fb} = F_{pm}\\
\phi_{fb} - \phi_{lfb} - \phi_{fb(t)} = 0\\
R_{fb(t)}\phi_{fb(t)} - R_{lfb}.\phi_{lfb} = 0
\end{aligned}\right\} \tag{8}$$

These equations can be written in the matrix form under unaligned condition,

$$\begin{bmatrix} R_{11} & 0 & 0 & 0 & R_{15} & 0 & 0\\ R_{21} & R_{22} & R_{23} & 0 & 0 & 0 & 0\\ 1 & -1 & 0 & 0 & -1 & 0 & 0\\ 0 & 1 & -1 & -1 & 0 & 0 & 0\\ R_{51} & R_{52} & 0 & R_{54} & 0 & 0 & 0\\ 0 & 0 & 0 & 1 & 0 & -1 & -1\\ 0 & 0 & 0 & 0 & 0 & R_{76} & R_{77} \end{bmatrix} \begin{bmatrix} \Phi_{pm}\\ \phi_{lg}\\ \phi_{sc}\\ \phi_{fb}\\ \phi_{lpma}\\ \phi_{lfb}\\ \phi_{fb(t)} \end{bmatrix} = \begin{bmatrix} F_{pm}\\ F_{pm}\\ 0\\ 0\\ F_{pm}\\ 0\\ 0 \end{bmatrix} \tag{9}$$

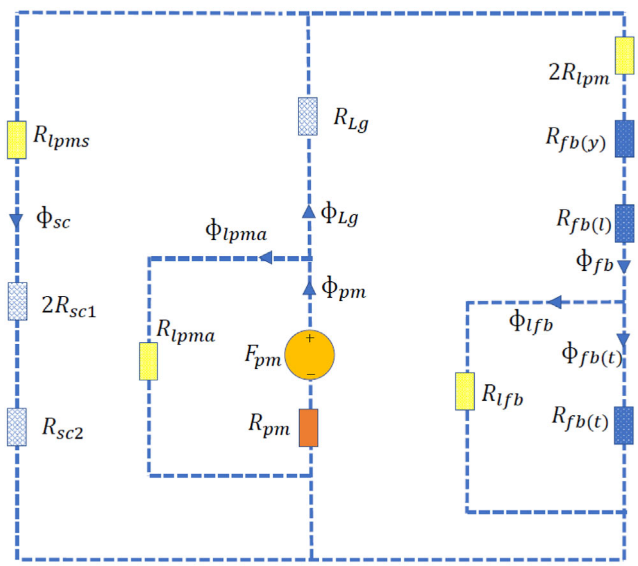

FIGURE 7. Simplified MERC of FB-TFPMG.

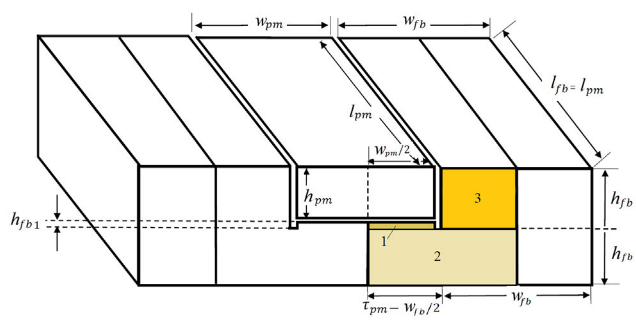

FIGURE 8. Isometric view of fall-back rotor.

where $R_{11} = R_{21} = R_{51} = R_{pm}$, $R_{15} = R_{lpma}$, $R_{22} = R_{52} = R_{lg}$, $R_{23} = 2R_{sc1} + R_{sc2} + R_{lpms}$ $R_{54} = R_{54} = (2R_{lpm} + R_{fb(l)} + R_{fb(y)} + +R_{fb(t)})$, $R_{76} = -R_{lfb}$, and $R_{77} = R_{fb(t)}$

Calculation of individual reluctances of different parts of FB-TFPMG are required to solve the above reluctance matrices. In the next section, the equations of the air-gap, fall-back rotor, stator cores, and leakage flux reluctances are derived.

3.3. Reluctance of the Fall-Back Rotor

Fall-back rotor of FB-TFPMG consists of three parts, i.e., rotor lower section, rotor yoke, and rotor upper section as shown in Figure 8. Fall-back rotor lower area (part 1 of the Figure 8) is an area under PM, rotor yoke area (part 2 of the Figure 8) is the bottom area of the rotor, and fall-back rotor upper area (part 3 of the Figure 8) is an area under the iron-bridge.

The reluctance of the fall-back rotor lower section $R_{fb(l)}$ is calculated as follows,

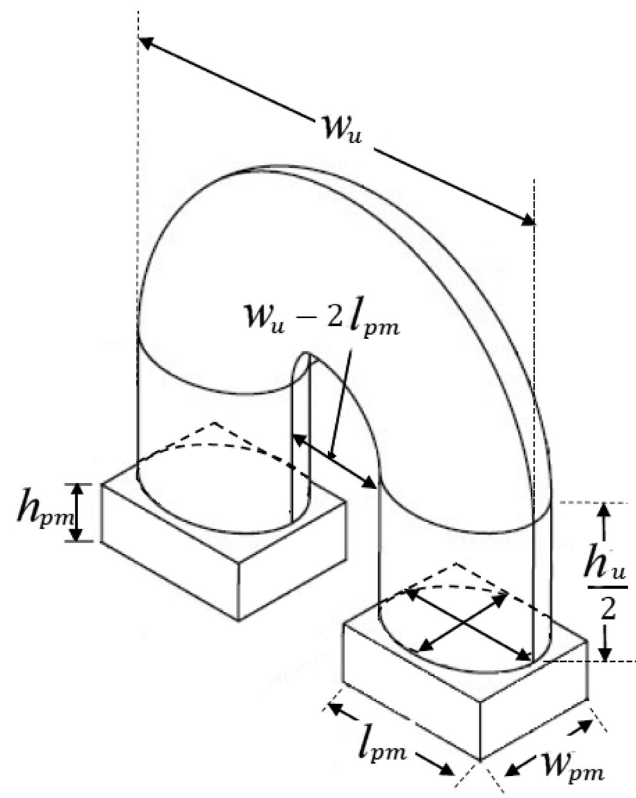

FIGURE 9. Elliptical U-shaped stator core.

$$R_{fb(l)} = \frac{2h_{fb1}}{\mu_0 \mu_{r(fb)} w_{pm} l_{fb}} \tag{10}$$

The reluctance of the fall-back rotor yoke $R_{fb(y)}$ is calculated using,

$$R_{fb(y)} = \frac{\tau_{pm}}{\mu_0 \mu_{r(fb)} h_{fb} l_{fb}} \tag{11}$$

The reluctance of fall-back rotor upper area $R_{fb(t)}$ is calculated using,

$$R_{fb(t)} = \frac{h_{fb}}{2\mu_0 \mu_{r(fb)} . w_{fb} . l_{fb}} \tag{12}$$

Therefore, the total reluctance of the fall-back rotor part is,

$$R_{fb} = 2(R_{fb(l)} + R_{fb(y)} + R_{fb(t)}/2) \tag{13}$$

3.4. Reluctance of the Elliptical U-Shaped Stator Core

The reluctance of the elliptical U-shaped stator core which is also made up of three parts as shown in Figure 9 is calculated as follows,

The reluctance of elliptical U-shaped stator core leg is calculated as,

$$R_{sc1} = \frac{4h_u}{\pi\mu_0\mu_{r(sc)}l_{pm}w_{pm}} \tag{14}$$

The reluctance of elliptical U-shaped stator upper core is calculated as,

$$R_{sc2} = \frac{\left(\pi\frac{(w_u-2l_{pm})+w_u}{4}\right)}{\pi\mu_0\mu_{r(sc)}l_{pm}w_{pm}} = \frac{(w_u - l_{pm})}{2\mu_0\mu_{r(sc)}l_{pm}w_{pm}} \tag{15}$$

Therefore, the total reluctance of the elliptical U-shaped stator core is

$$R_{sc} = 2R_{sc1} + R_{sc2} \tag{16}$$

3.5. Air-Gap Reluctance

With respect to the rotor position of the FB-TFPM generator, air-gap reluctance is also varied. The equivalent magnetic reluctance of air-gap during aligned condition, without fringing effect is,

$$R_{lg(align)} = \frac{l_g}{\mu_0.l_{pm}.w_{pm}} \tag{17}$$

The air-gap magnetic reluctance including the fringing effect can be computed by

$$R_{lg(align)} = \frac{l_g}{\mu_0(w_{pm}+2l_f).(l_{pm}+2l_f)} \tag{18}$$

where l_f is the length of the fringing flux path.

For the fully unaligned condition, the equivalent magnetic reluctance of the air-gap without the fringing effect can be computed for a single pole as,

$$R_{lg(\text{unalign})} = \frac{l_g}{\mu_0.l_{fb}.w_{fb}} \tag{19}$$

where l_{fb}, w_{fb}, l_g, and $R_{lg(\text{unalign})}$ are the axial length of the fall-back rotor, radial width of the fall-back rotor, air-gap length, and air-gap reluctance in unaligned condition of PM poles and stator core, respectively.

The equivalent magnetic reluctance of the air-gap in unaligned condition by considering the fringing effect can by computed by

$$R_{lg(\text{unalign})} = \frac{l_g}{\mu_0(w_{fb}+2l_f).(l_{fb}+2l_f)} \tag{20}$$

3.6. Leakage Permeance Calculations

The own leakage permeance due to the PMs as shown in Figure 10, between the two fall-back part is given by paths 1 and 2.

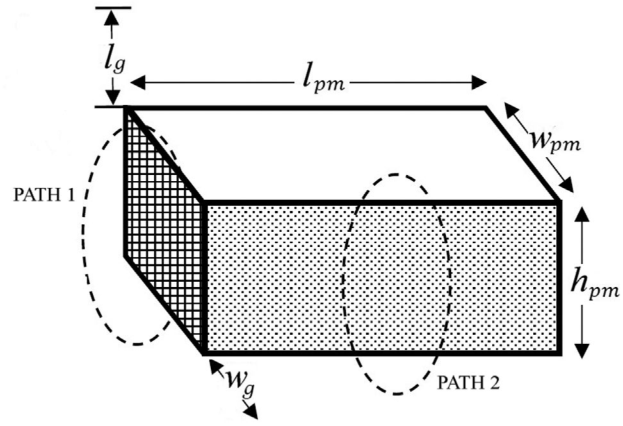

FIGURE 10. Leakage flux due to active PMs.

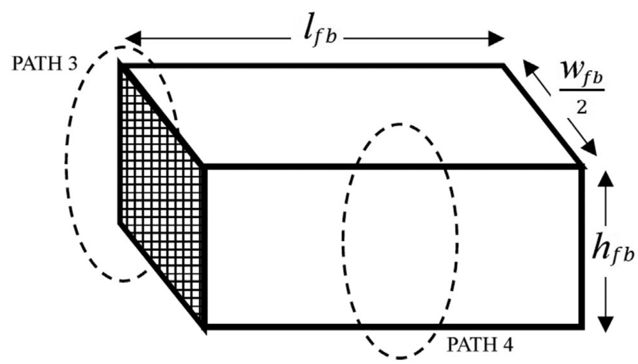

FIGURE 11. Leakage flux due to fall-back rotor.

$$\mathcal{P}_{lpma1} = \mu_0.w_{pm}\int_0^{\frac{l_{pm}}{2}} \frac{dx}{(2\pi x + h_{pm})} \tag{21}$$

which leads to

$$\mathcal{P}_{lpma1} = \frac{\mu_0.w_{pm}}{2\pi}.\ \ln\left(\frac{2\pi l_{pm}}{h_{pm}} + 1\right) \tag{22}$$

similarly, for path 2, the flux leakages between the gap of two adjacent poles (w_g) in the radial direction,

$$\mathcal{P}_{lpma2} = \mu_0.l_{pm}\int_0^{\frac{w_{pm}}{2}} \frac{dx}{(\pi x + w_g)} \tag{23}$$

$$\mathcal{P}_{lpma2} = \frac{\mu_0.l_{pm}}{\pi}.\ \ln\left(\frac{\pi w_{pm}}{w_g} + 1\right) \tag{24}$$

The total leakage flux Permeance due to the active PMs is

$$\mathcal{P}_{lpma} = 2\mathcal{P}_{lpma1} + 2\mathcal{P}_{lpma2} \tag{25}$$

In FB-TFPMG, as inactive magnets are replaced by fall-back rotor part, the leakage flux due to fall-back rotor part

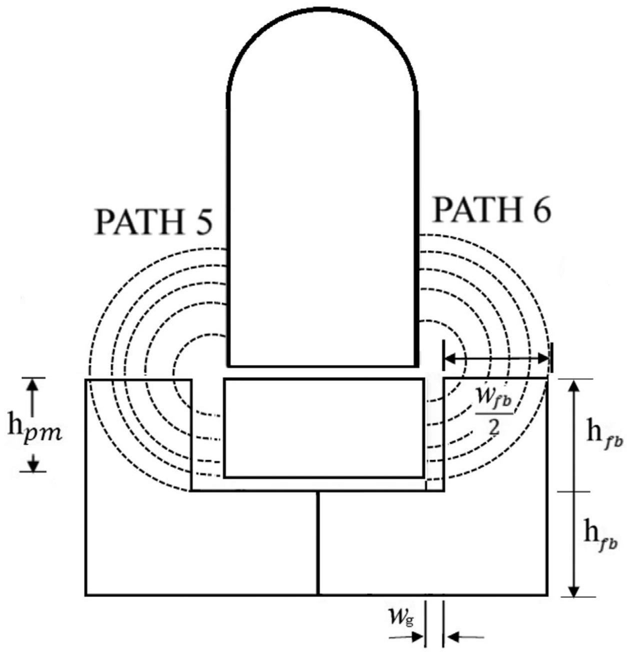

FIGURE 12. Lateral leakage fluxes between the fall-back rotor part and the U-shaped stator.

as shown in Figure 11, is given by paths 3 and 4. In one pole pair of MERC, only half of the fall-back rotor poles is considered, and hence, the side leakage fluxes are not incorporated.

$$\mathcal{P}_{lfb3} = \mu_0 . \frac{w_{fb}}{2} \int_0^{\frac{l_{fb}}{2}} \frac{dx}{(2\pi x + h_{fb})} \tag{26}$$

$$\mathcal{P}_{lfb3} = \frac{\mu_0 . w_{fb}}{4\pi} . \ \ln\left(\frac{\pi l_{fb}}{h_{fb}} + 1\right) \tag{27}$$

similarly, for path 4,

$$\mathcal{P}_{lfb4} = \mu_0 . l_{fb} \int_0^{\frac{w_{fb}}{2}} \frac{dx}{(2\pi x + h_{fb})} \tag{28}$$

$$\mathcal{P}_{lfb4} = \frac{\mu_0 . l_{fb}}{2\pi} . \ \ln\left(\frac{\pi w_{fb}}{h_{fb}} + 1\right) \tag{29}$$

The total leakage permeance due to the fall-back rotor is

$$\mathcal{P}_{lfb} = \mathcal{P}_{lfb3} + \mathcal{P}_{lfb4} \tag{30}$$

Lateral leakage fluxes between fall-back rotor part and elliptical U-shaped stator core are shown in Figure 12. These leakage fluxes reduce the flux linkages of stator coil, therefore it is important to evaluate the leakage flux permeance between the active PMs and elliptical U-shaped stator core, which are represented by paths 5 and 6.

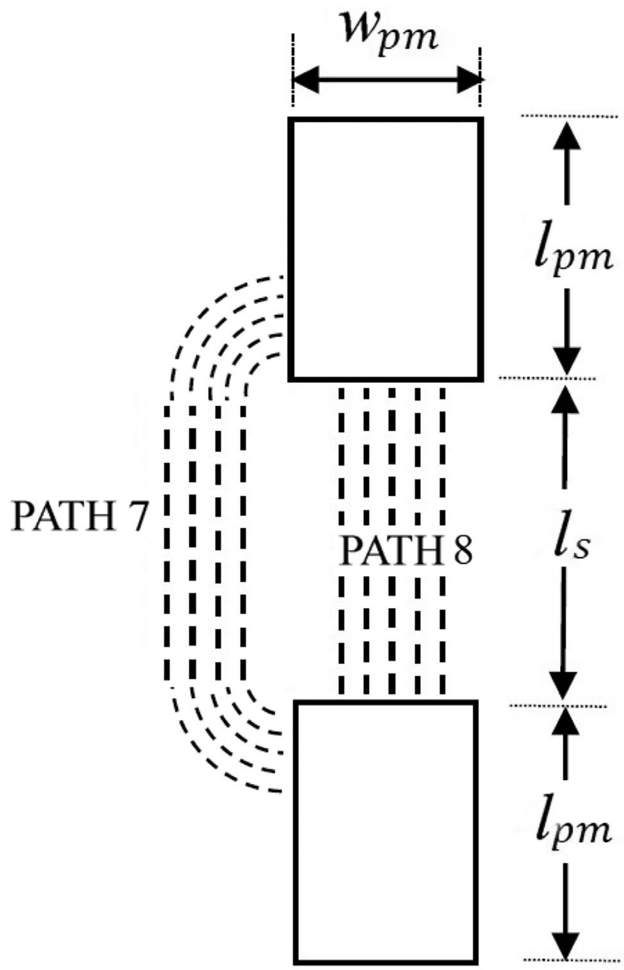

FIGURE 13. Leakage fluxes between the two active PMs placed between the two fall-back rotors.

$$\mathcal{P}_{lpms5} = \mu_0 \mu_r . l_{pm} \int_0^{h_{pm}} \frac{dx}{\left(\frac{\pi}{2} x + l_g + 2w_g\right)} \tag{31}$$

$$\mathcal{P}_{lpms5} = \frac{2\mu_0 \mu_r . l_{pm}}{\pi} \ \ln\left(\frac{\pi h_{pm}}{2(l_g + 2w_g)} + 1\right) \tag{32}$$

Similarly, $\mathcal{P}_{lpms6}$ can be calculated and the total lateral leakage flux between the fall-back rotor and the U-shaped stator core is

$$\mathcal{P}_{lpms} = \mathcal{P}_{lpms5} + \mathcal{P}_{lpms6} \tag{33}$$

Leakage fluxes between the two active PMs placed between the two fall-back rotor parts as shown in Figure 13, are given by paths 7 and 8.

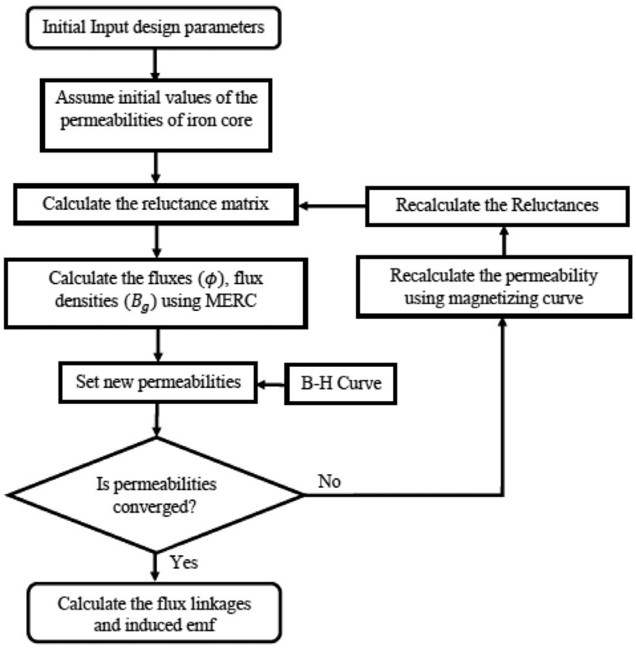

FIGURE 14. Flow chart representing the process of design optimization of the FB-TFPMG.

$$\mathcal{P}l_{pm7} = \mu_0\mu_r h_{pm}\int_0^{\frac{l_{pm}}{2}} \frac{dx}{\left(\frac{\pi}{2}x + l_s\right)} \tag{34}$$

$$\mathcal{P}_{lpm7} = \frac{2\mu_0\mu_r h_{pm}}{\pi}.\ \ln\left(\frac{\pi l_{pm}}{4l_s} + 1\right) \tag{35}$$

The direct leakage permeance (path 8) between PMs can be calculated,

$$\mathcal{P}l_{pm8} = \mu_0\mu_r w_{pm}\int_0^{h_{pm}} \frac{dx}{(l_s)} = \mu_0.w_{pm}\ \ln\left(\frac{1}{l_s}\right) \tag{36}$$

The total leakage fluxes between the two active PMs placed are calculated by multiplying the total number of pole pairs.

3.7. Reluctance of PMs

The reluctance of each PM can be calculated as,

$$R_{pm} = \frac{h_{pm}}{\mu_0\mu_{r(pm)}w_{pm}l_{pm}} \tag{37}$$

where h_{pm} is the height of the PM, w_{pm} is the width of the PM, and l_{pm} is the length of the PM.

3.8. Flux Calculations

The PMs are the *mmf* source in this magnetic circuit and can be modeled as,

$$F_{pm} = h_{pm}.H_c \tag{38}$$

F_{pm} can be written as,

$$F_{pm} = \frac{B_{r(pm)}.h_{pm}}{\mu_0.\mu_{r(pm)}} \tag{39}$$

where $B_{r(pm)}$ and $\mu_{r(pm)}$ are the magnet remanent flux density and magnet relative permeability, respectively. $\mu_{r(pm)}$ is nearly equal to the relative permeability of air. Therefore, the PM flux can be calculated from

$$\phi_{pm} = \frac{B_{r(pm)}.h_{pm}}{\mu_0\mu_{r(pm)}R_{pm}} \tag{40}$$

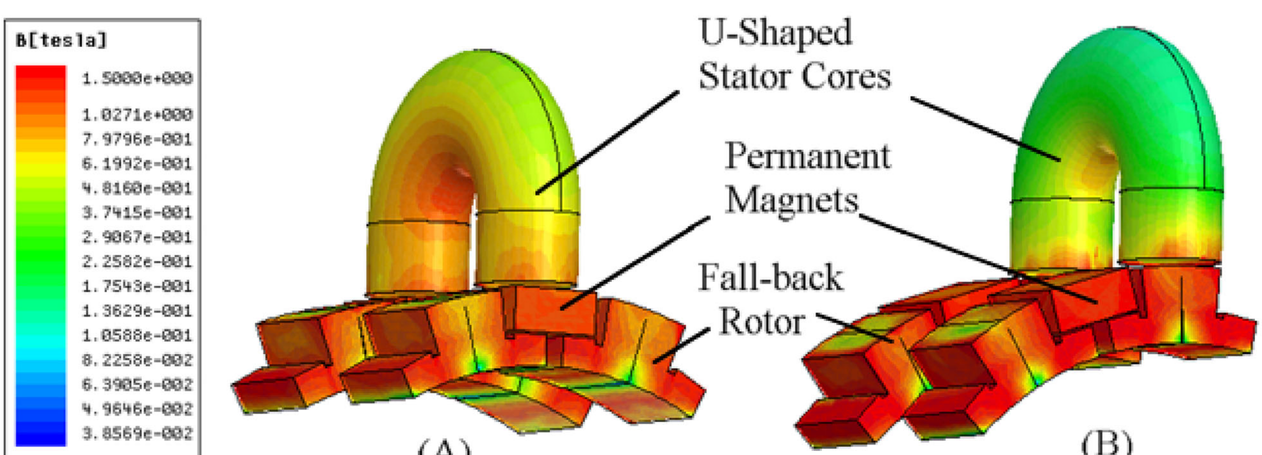

FIGURE 15. Flux density plot of one pole of FB-TFPMG (A) Aligned condition of rotor PM and stator core, and (B) Unaligned condition of rotor PM and stator core.

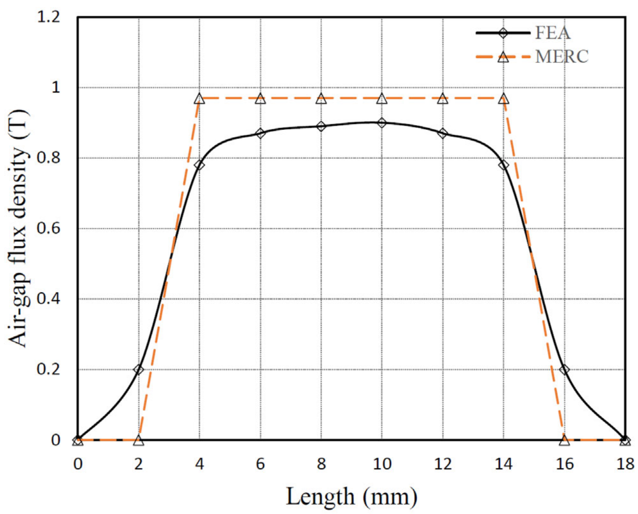

FIGURE 16. Air-gap flux density of one pole of FB-TFPMG under aligned condition.

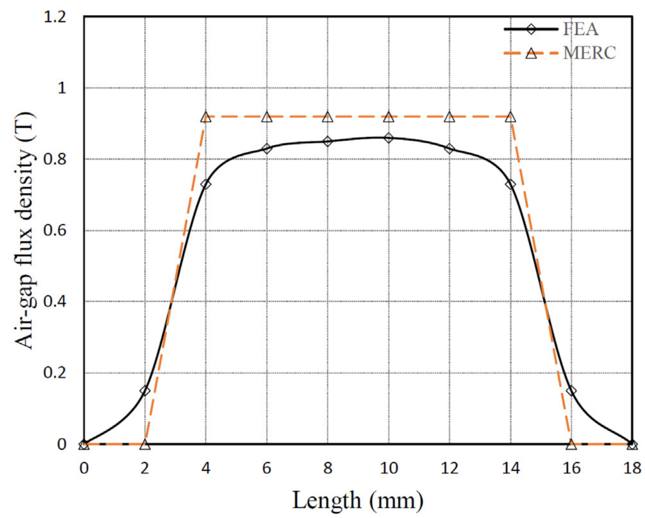

FIGURE 17. Air-gap flux density of one pole of FB-TFPMG under unaligned condition.

The reluctance of PM, $R_{pm} = 2.1095.10^7$ AT/Wb and reluctance of stator core, $= 2.5407.10^7$ AT/Wb are calculated. Subsequently all the required reluctances are calculated, and fluxes through various part of the FB-TFPMG are calculated.

The magnetic saturation deteriorates the electromagnetic performance of FB-TFPMG and increases losses. To overcome the limitation of nonlinear characteristics, various algorithms have been proposed in Ref. [36]. For precise estimation of results when the machine saturates, a nonlinear model is required for the MERC. The B-H curve of the iron material used for the core is integrated in the iterative process. As a result, an iterative procedure is carried out to specify the permeability of the iron parts in accordance with the flow chart shown in Figure 14. The volume optimization of the inner rotor FB-TFPMG is performed by means of a parameter sweep method over various key parameters. The magnet height H_{pm}, width W_{pm}, and length L_{pm} parameters determine the main dimensions of the machine. The limiting factor of increasing the value of H_{pm} is the saturation of the core and the overall dimensions can be affected due to increase in the height of the magnet The magnet height is limited to $5 \leq H_{pm} \leq 8$ mm. An iterative approach is used to update the reluctance matrix and to determine the flux in air-gap by magnetic equivalent circuit using the updated reluctance matrix. To start with, a converged value of the core relative permeability is estimated and then, magnetic flux densities are determined. Fluxes under aligned and unaligned conditions between rotor PMs and stator core are tabulated in the Table 2.

Particular (Wb)	Aligned	Unaligned
ϕ_{pm}	299.7	299.7
ϕ_{lg}	234.9	241.4
ϕ_{plma}	65	59
ϕ_{fb}	223	238.8
ϕ_{sc}	162.2	157.1
ϕ_{lpms}	54	49
ϕ_{lfb}	59	55

TABLE 2. The no-load fluxes [$.10^{-6}$].

4. RESULT AND DISCUSSION

The magnetic flux densities under aligned and unaligned conditions are obtained analytically for the inner rotor FB-TFPMG. To validate the analytical results, a 3D-FEA time varying (transient) analysis was carried out. Due to symmetry only one fourth of the whole model was analyzed at different rotor position. Figure 15 shows the flux density plot of the one pole pair with the stator core. The magnetic field pattern of air-gap has been analyzed under aligned and unaligned conditions and

Parameters	Aligned condition FE	Analytical	Unaligned condition FE	Analytical
B_{pm}	1.20	1.24	1.16	1.24
B_g	0.90	0.98	0.87	0.92
B_{sc}	0.83	0.86	0.79	0.83
B_{fb}	0.89	0.95	0.91	0.99

TABLE 3. Comparison of FE and analytical results of flux densities under no-load condition.

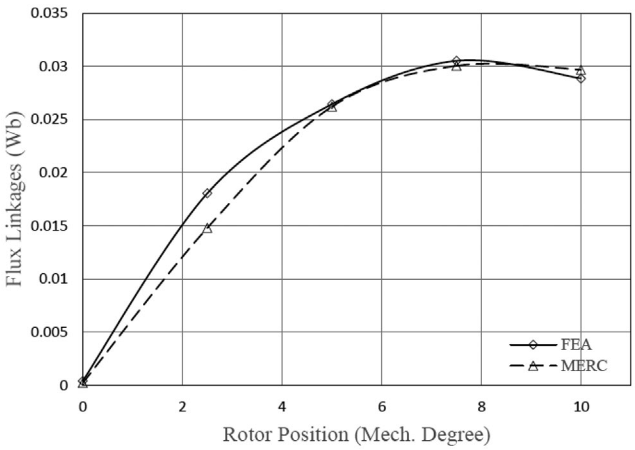

FIGURE 18. Comparison of flux linkages of FB-TFPMG.

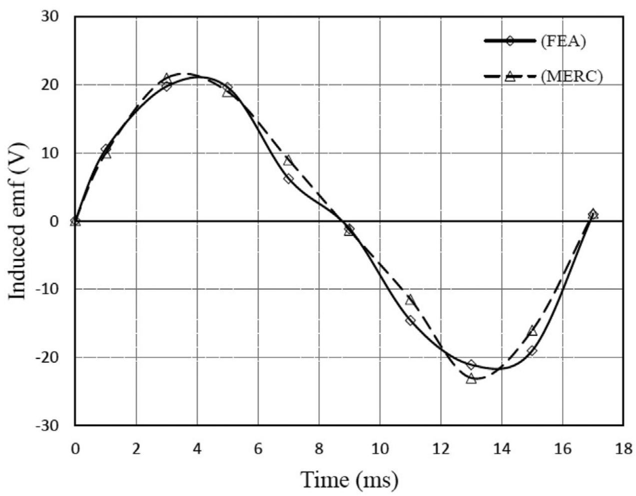

FIGURE 19. Comparison of induced emf plot of FB-TFPMG.

depicted in Figures 16 and 17. Line of arcs were drawn at the place of air-gap, where the flux densities are to be found and their plots are compared by both the methods. As it can be observed that the distribution of the flux per unit area between the active magnetic PM pole and the U-shaped stator core area is almost uniform. The FE analysis of flux densities under both aligned and unaligned conditions are compared with analytical results in Table 3. The reported results of MERC can be seen comparable to the results of FE based simulations.

Figure 18 shows the comparison of flux linkages obtained through analytical and FEA and Figure 19 shows the comparison of induced emf.

5. CONCLUSION

The inner rotor FB-TFPMG utilizes half the PMs and U-shaped elliptical stator core in comparison with the conventional TFPMG, resulting in lower construction cost and higher power density. The improvement is a major benefit of utilizing only active PMs and excluding the usage of nonactive PMs. An analytical model using magnetic equivalent reluctance network is derived for inner rotor FB-TFPMG configuration and simplified the circuit under two different conditions, i.e., aligned and unaligned condition. The analytical MERC is developed with detailed modeling for air-gap, fall-back rotor, and U-shaped stator core flux path. Fall-back rotor, elliptical U-shaped stator core, PMs, and air-gap reluctances are calculated and hence flux densities. The concept presented with fall-back rotor topology is analyzed through time-stepping analysis in 3D FEA tool. The results of air-gap flux densities of FE analysis are compared with analytical results and are in good agreement within the range of 7% variation.

ORCID

Mahesh A. Patel http://orcid.org/0000-0003-0342-0038
Santosh C. Vora http://orcid.org/0000-0002-4017-0843

REFERENCES

[1] S. Toledo, M. Rivera, and J. L. Elizondo, “Overview of wind energy conversion systems development, technologies and power electronics research trends,” presented at the 2016 IEEE International Conference on Automatica (ICA-ACCA), Curico, Chile, 2016, pp. 1–6. DOI: 10.1109/ICA-ACCA.2016.7778454.

[2] D. Je Bang, H. Polinder, G. Shrestha, and J. A. Ferreira, “Promising direct-drive generator system for large wind turbines,” *EPE J.*, vol. 18, no. 3, pp. 7–13, 2008. DOI: 10.1080/09398368.2008.11463683.

[3] A. Chen, R. Nilssen, and A. Nysveen, “Performance comparisons among radial-flux, multistage axial-flux, and three-phase transverse-flux pm machines for downhole applications,” *IEEE Trans. Ind. Appl.*, vol. 46, no. 2, pp. 779–789, 2010. DOI: 10.1109/TIA.2009.2039914.

[4] M. Liserre, R. Cárdenas, M. Molinas, and J. Rodriguez, “Overview of multi-mw wind turbines and wind parks,” *IEEE Trans. Ind. Electron*, vol. 58, no. 4, pp. 1081–1095, 2011. DOI: 10.1109/TIE.2010.2103910.

[5] Y. Chen, P. Pillay, and A. Khan, “Pm wind generator topologies,” *IEEE Trans. Ind. Appl.*, vol. 41, no. 6, pp. 1619–1626, 2005. DOI: 10.1109/TIA.2005.858261.

[6] H. Polinder et al., “Trends in wind turbine generator systems,” *IEEE J. Emerg. Sel. Top. Power Electron.*, vol. 1, no. 3, pp. 174–185, 2013. DOI: 10.1109/JESTPE.2013.2280428.

[7] H. Polinder, F. van der Pijl, G.-J. de Vilder, and P. Tavner, “Comparison of direct-drive and geared generator concepts for wind turbines,” *IEEE Trans. Energy Convers.*, vol. 21, no. 3, pp. 725–733, 2006. DOI: 10.1109/TEC.2006.875476.

[8] R. S. Semken, “Direct-drive permanent magnet generators for high-power wind turbines: Benefits and limiting factors,” *IET Renew. Power Gener.*, vol. 6, no. 7, pp. 1–8, Jan. 2012.

[9] K. Ma, L. Tutelea, I. Boldea, D. M. Ionel, and F. Blaabjerg, “Power electronic drives, controls, and electric generators for large wind turbines–an overview,” *Electr. Power Compon. Syst.*, vol. 43, no. 12, pp. 1406–1421, 2015. DOI: 10.1080/15325008.2015.1037470.

[10] Z. Chen and H. Li, “Overview of different wind generator systems and their comparisons,” *IET Renew. Power Gener.*, vol. 2, no. 2, pp. 123–138, Jun. 2008. DOI: 10.1049/iet-rpg:20070044.

[11] Y. Guo, J. G. Zhu, P. Watterson, and W. Wu, “Development of a pm transverse flux motor with soft magnetic composite core,” *IEEE Trans. Energy Convers.*, vol. 21, no. 2, pp. 426–434, 2006. DOI: 10.1109/TEC.2005.860403.

[12] R. Nasiri-Zarandi, A. M. Ajamloo, and K. Abbaszadeh, “Design optimization of a transverse flux halbach-array pm generator for direct drive wind turbines,” *IEEE Trans. Energy Convers.*, vol. 35, no. 3, pp. 1485–1493, 2020. DOI: 10.1109/TEC.2020.2975259.

[13] R. Kumar *et al.*, “Impact of magnetic coupling in transverse flux permanent magnet machine for wind power application,” presented at the 10th International Conference on Power Electronics, Machines and Drives (PEMD 2020), Online Conference, 2020, pp. 759–764. DOI: 10.1049/icp.2021.1007.

[14] J. R. Anglada, “Analytical calculation of the torque produced by transverse flux machines,” *IET Electr. Power Appl.*, vol. 11, no. 7, pp. 1298–1305, Aug. 2017.

[15] S. Taravat, A. Kiyoumarsi, and N. Bracikowski, “Mitigation of cogging torque in transverse-flux permanent-magnet machines with flux concentrators by step skewing of stator pole,” *IET Electr. Power Appl.*, vol. 14, no. 12, pp. 2378–2388, Dec. 2020. DOI: 10.1049/iet-epa.2020.0029.

[16] M. el Hadi Bendib, M. Hachemi, and F. Marignetti, “Electromagnetic design and analysis of a novel axial-transverse flux permanent magnet synchronous machine,” *Electr. Power Compon. Syst.*, vol. 45, no. 8, pp. 912–924, 2017. DOI: 10.1080/15325008.2017.1310954.

[17] T. Husain, I. Hasan, Y. Sozer, I. Husain, and E. Muljadi, “A comprehensive review of permanent magnet transverse flux machines for direct drive applications,” presented at the 2017 IEEE Energy Conversion Congress and Exposition (ECCE), Cincinnati, OH, USA, 2017, pp. 1255–1262. DOI: 10.1109/ECCE.2017.8095933.

[18] D. Bang, H. Polinder, G. Shrestha, and J. A. Ferreira, “Design of a lightweight transverse flux permanent magnet machine for direct-drive wind turbines,” presented at the 2008 IEEE Industry Applications Society Annual Meeting, Edmonton, AB, Canada, 2008, pp. 1–7. DOI: 10.1109/08IAS.2008.71.

[19] O. Dobzhanskyi, R. Gouws, and E. Amiri, “Comparison analysis of AC PM transverse-flux machines of different designs in terms of power density and cost,” presented at the 2017 IEEE 58th International Scientific Conference on Power and Electrical Engineering of Riga Technical University (RTUCON), Riga, Latvia, 2017, pp. 1–6. DOI: 10.1109/RTUCON.2017.8124762.

[20] H. Yao, H. Li, and K. Wang, “Design and optimization of a concentrated flux transverse flux permanent motor,” presented at the 2016 IEEE 8th International Power Electronics and Motion Control Conference (IPEMC-ECCE Asia), Hefei, 2016, pp. 3018–3021. DOI: 10.1109/IPEMC.2016.7512777.

[21] A. Darabi, H. Tahanian, A. Alaeddini, and R. Mirzahosseini, “Steps towards a sinusoidal back EMF for a claw pole transverse flux permanent magnet synchronous machine,” presented at the 4th Annual International Power Electronics, Drive Systems and Technologies Conference, Tehran, Iran, 2013, pp. 328–332. DOI: 10.1109/PEDSTC.2013.6506727.

[22] F. T. V. Nica, E. Ritchie, and K. Leban, “A comparison between two optimized TFPM geometries for 5 MW direct-drive wind turbines,” presented at the 2013 8th International Symposium on Advanced Topics in Electrical Engineering (ATEE), Bucharest, Romania, 2013, pp. 1–6. DOI: 10.1109/ATEE.2013.6563501.

[23] Y. Gong, W. Zheng, D. Zhang, and J. Jiang, “Analysis of a transverse flux machine with E-shaped stator using three dimensional scalar potential finite element method,” presented at the 2009 IEEE 6th International Power Electronics and Motion Control Conference, Wuhan, China, 2009, pp. 1991–1994. DOI: 10.1109/IPEMC.2009.5157721.

[24] M. Zafarani, M. Moallem, and A. Tabesh, “Analytical model for a transverse flux permanent magnet machine using improved magnetic equivalent circuit approach,” presented at the 2011 21st International Conference on Systems Engineering, Las Vegas, NV, USA, 2011, pp. 96–99. DOI: 10.1109/ICSEng.2011.25.

[25] M. A. Patel and S. C. Vora, “Analysis of a fall-back transverse-flux permanent-magnet generator,” *IEEE Trans. Magn.*, vol. 53, no. 11, pp. 1–5, 2017. DOI: 10.1109/TMAG.2017.2702745.

[26] M. F. Kremers, J. J. Paulides, and E. A. Lomonova, “Toward accurate design of a transverse flux machine using an analytical 3-D magnetic charge model,” *IEEE Trans. Magn.*, vol. 51, no. 11, pp. 1–4, 2015. DOI: 10.1109/TMAG.2015.2444994.

[27] O. Dobzhanskyi, E. E. Mendrela, and A. M. Trzynadlowski, “Analysis of leakage flux losses in the transverse flux permanent magnet generator,” presented at the 2011 IEEE Green Technologies Conference (IEEE-Green), Baton Rouge, LA, USA, 2011, pp. 1–6. DOI: 10.1109/GREEN.2011.5754883.

[28] I. Hasan *et al.*, “Analytical modeling of a novel transverse flux machine for direct drive wind turbine applications,” presented at the 2015 IEEE Energy Conversion Congress and Exposition (ECCE), Montreal, QC, Canada, 2015, pp. 2161–2168. DOI: 10.1109/ECCE.2015.7309965.

[29] A. McDonald and N. A. Bhuiyan, “On the optimization of generators for offshore direct drive wind turbines,” *IEEE Trans. Energy Convers.*, vol. 32, no. 1, pp. 348–358, 2017. DOI: 10.1109/TEC.2016.2624219.

[30] J. Faiz, H. Nejadi-Koti, and A. H. Exiri, “Inductance-based inter-turn fault detection in permanent magnet synchronous machine using magnetic equivalent circuit model,” *Electr. Power Compon. Syst.*, vol. 45, no. 9, pp. 1016–1030, 2017. DOI: 10.1080/15325008.2017.1293196.

[31] P. Naderi, S. Sharouni, and M. Moradzadeh, “Analysis of partitioned stator flux-switching permanent magnet machine by magnetic equivalent circuit,” *Int. J. Elect. Power Energy Syst.*, vol. 111, pp. 369–381, 2019. DOI: 10.1016/j.ijepes.2019.04.022.

[32] M. A. Patel and S. C. Vora, "Analysis of a transverse flux permanent magnet generator with fall-back outer rotor design for wind power generation," *Int. J. Ambient Energy*, vol. 41, no. 11, pp. 1308–1313, 2020. DOI: 10.1080/01430750.2018.1507948.

[33] L. Boldea, *Variable Speed Generators*. CRC Press, Taylor and Francis Group, 2015, pp. 479–526.

[34] A. A. Pourmoosa and M. Mirsalim, "A transverse flux generator with a single row of permanent magnets: Analytical design and performance evaluation," *IEEE Trans. Ind. Electron.*, vol. 66, no. 1, pp. 152–161, 2019. DOI: 10.1109/TIE.2018.2831179.

[35] A. A. Pourmoosa, M. Mirsalim, A. Mahmoudi, and S. Vaez-Zadeh, "Analytical model based on magnetic equivalent circuit for transverse-flux permanent-magnet machines," *Int. Trans. Electr. Energy Syst.*, vol. 30, no. 7, pp. e12414, 2020. DOI: 10.1002/2050-7038.12414.

[36] K. Vanchinathan, K. R. Valluvan, C. Gnanavel, and C. Gokul, "Numerical simulation and experimental verification of fractional-order PI $^{\lambda}$ controller for solar PV fed sensorless brushless DC motor using whale optimization algorithm," *Electr. Power Compon. Syst.*, vol. 50, no. 1–2, pp. 64–80, 2022.

BIOGRAPHIES

Mahesh A. Patel received the M. Tech. in Electrical Engineering with specialization in Power Apparatus & Systems from Institute of Technology, Nirma University, Ahmedabad, Gujarat, India in 2008 and Ph. D. degree in Electrical Engineering from the Department of Electrical Engineering, Institute of Technology, Nirma University, Ahmedabad. At present, he is working as an Assistant Professor in the Department of Electrical Engineering, Institute of Technology, Nirma University, Ahmedabad. His research area includes design and analysis of advanced electrical machines, modeling of electrical machines and finite element analysis.

Santosh C. Vora (SM '21) was born in 1974. He received the B.E. degree in electrical engineering from Saurashtra University, Rajkot, India, in 1997 and the M.E. and Ph.D. degree in electrical engineering with specialization in high-voltage engineering from the Indian Institute of Science (IISc), Bangalore, in 2004 and 2009 respectively. At present, he is working as Professor in the Dept. of Electrical Engineering, Institute of Technology, Nirma University, Ahmedabad. His research areas include power system analysis, effect of inclusion of renewable systems in the conventional power system, advanced electrical machines and high-voltage measurement related instrumentation and diagnostics.